

winds infinitely rapidly around  $X^*$ , so to prevent computation divergence, interpolation is interrupted whenever an interfacial element cycles around  $X^*$ . This has the physical interpretation that material granularity causes particles near  $X^*$  to simply rotate in place<sup>27,28</sup>.

Results from both model and experiments are summarized in Fig. 3. In the main plot, we show three measures of chaotic stretching. First, as filled circles, we plot the number of pixels,  $\Delta$ , (normalized so that  $\Delta = 1$  across the vessel diameter) bordering green and red regions in the photographs shown in Fig. 1a as a function of the number of rotations,  $n$ , of the experimental cylinder. Second, as a thin line, we plot the calculated length (again normalized to the vessel diameter) of the same interface from the model whose results are summarized in Fig. 1b. Each of these measures extends from 0 to 1 complete revolution of the tumbler. Third, we compute a longer-time stretching rate<sup>29</sup> by evolving a very short line segment (length  $\Delta_0 = 0.00005D$ ) 10 revolutions forward in time, rescaling the length to  $\Delta_0$  whenever it grows above  $0.005D$ . In Fig. 3, we show in grey the growth starting from an initial condition centred on the line of symmetry through the granular bed at a radius  $r = 0.375D$ . This initial condition is used as an illustration because it produces a stretching rate (that is, the slope,  $K$ , of  $\log(\Delta)$  versus  $n$ ) close to the average,  $\langle K \rangle = 3.7$  revolutions<sup>-1</sup>, that one obtains from a uniform distribution of initial conditions along the symmetry line.  $K$  ranges from 0 to 8.7, with the smallest values near  $X^*$ , where the periodic perturbation traps particles, and near the cylinder walls, where (for low fill) particles seldom reach the flowing layer.

These three data sources are each fitted with an exponential function, giving stretching rates of  $3 \pm 2$ ,  $5 \pm 0.3$  and  $3.82 \pm 0.09$  revolutions<sup>-1</sup>, respectively. In each case the stretching rate is unambiguously positive, consistent with exponential stretching over several orders of magnitude in only one or two tumbler revolutions. For comparison, in Fig. 3 bottom right inset, we plot on a linear scale the stretching of the same interface in the model with (solid curve) and without (broken curve) periodic stick-slip. (Behaviour without stick-slip corresponds to  $A = 0$  in equation (2).) As anticipated, in a single revolution the periodically driven case exhibits strongly nonlinear interfacial stretching over two orders of magnitude, whereas the unforced case grows linearly with time, accounting for only one order of magnitude of interfacial stretching.

Evidently fine powders, like fluids, can spontaneously mix chaotically, at rates overwhelmingly exceeding those possible by the mechanisms expected from studies of freely flowing grains. Neither the spontaneous occurrence of the chaotic patterns studied here, nor the potential for exponential mixing rates, has been reported previously. From the fundamental standpoint, it seems clear that we still have much to learn about granular dynamics, as evidenced by the apparent connection between microscopic dynamics (which initiate stick-slip behaviour) and macroscopic transport (manifested by the intricate mixing patterns that we have reported). From the practical standpoint, the results of mixing studies of coarse grains clearly cannot be applied to the blending of fine or cohesive powders, which are widely used industrially. The challenge for the future will be to understand, from an applied perspective, how to exploit the connection between micro- and macro-scale granular dynamics to obtain improvements in mixing times which amount to tens of orders of magnitude. □

Received 9 October 1998; accepted 12 January 1999.

1. Thorpe, S. A. Experiments on the instability of stratified shear flows: miscible fluids. *J. Fluid Mech.* **46**, 299–319 (1971).
2. Van Dyke, M. (ed.) *An Album of Fluid Motion* (Parabolic, Stanford, California, 1982).
3. Taylor, G. I. Stability of a viscous liquid contained between two rotating cylinders. *Phil. Trans. R. Soc. Lond. A* **223**, 289–343 (1923).
4. Andereck, C. D., Liu, S. S. & Swinney, H. L. Flow regimes in a circular Couette system with independently rotating cylinders. *J. Fluid Mech.* **164**, 155–183 (1986).
5. Solomon, T. H. & Gollub, J. P. Chaotic particle transport in time-dependent Rayleigh-Bénard convection. *Phys. Rev. A* **38**, 6280–6284 (1988).
6. Aref, H. Stirring by chaotic advection. *J. Fluid Mech.* **143**, 1–21 (1984).

7. Alvarez, M. M., Muzzio, F. J., Cerbelli, S., Androver, A. & Giona, M. Self-similar spatio-temporal structure of material filaments in chaotic flows. *Phys. Rev. Lett.* **81**, 3395–3398 (1998).
8. Lamberto, D. J. & Muzzio, F. J. Experimental and computational investigation of the laminar flow structure in a stirred tank. *Chem. Eng. Sci.* (in the press).
9. Hobbs, D. M., Alvarez, M. M. & Muzzio, F. J. Mixing in globally chaotic flows: a self-similar process. *Fractals* **5**, 395–428 (1997).
10. Choo, K., Molteni, T. C. A. & Morris, S. W. Traveling granular segregation patterns in a long drum mixer. *Phys. Rev. Lett.* **79**, 2975–2977 (1997).
11. Metcalf, G., Shinbrot, T., McCarthy, J. J. & Ottino, J. M. Avalanche mixing of granular solids. *Nature* **374**, 39–41 (1995).
12. Wightman, C., Mort, P. R., Muzzio, F. J., Riman, R. E. & Gleason, E. K. The structure of mixtures of particles generated by time-dependent flows. *Powder Technol.* **84**, 231–240 (1995).
13. Brone, D. et al. Using flow perturbations to enhance mixing of dry powders in V-blenders. *Powder Technol.* **91**, 165–172 (1997).
14. Khakhar, D. V., McCarthy, J. J., Shinbrot, T. & Ottino, J. M. Transverse flow and mixing of granular materials in a rotating cylinder. *Phys. Fluids* **9**, 31–43 (1997).
15. Van Cleef, J. Powder technology. *Am. Sci.* **79**, 304–315 (1991).
16. Gupta, S. D., Khakhar, D. V. & Bhatia, S. K. Axial segregation of particles in a horizontal rotating cylinder. *Chem. Eng. Sci.* **46**, 1513–1525 (1991).
17. Hill, K. M., Caprihan, A. & Kakalios, J. Bulk segregation in rotated granular material measured by magnetic resonance imaging. *Phys. Rev. Lett.* **78**, 50–53 (1997).
18. Pouliquen, O., Delour, J. & Savage, S. B. Fingering in granular flows. *Nature* **386**, 816–817 (1997).
19. Nakagawa, M., Altobelli, S. A., Caprihan, A., Fukushima, E. & Jeong, E. K. Non-invasive measurements of granular flows by magnetic resonance imaging. *Exp. Fluids* **16**, 54–60 (1993).
20. Campbell, H. & Bauer, W. C. Cause and cure of demixing in solid-solid mixers. *Chem. Eng.* **179**–185 (1966).
21. Chester, A. W. et al. Mixing dynamics in catalyst impregnation in twin-cone blenders. *Powder Technol.* (in the press).
22. Moakher, M., Shinbrot, T. & Muzzio, F. J. Experimentally validated computations of flow, mixing and segregation of non-cohesive grains in 3D tumbling blenders. (preprint, Rutgers Univ., Piscataway, New Jersey 08854 USA, 1998).
23. Nasono, S., Kudrolli, A. & Gollub, J. P. Friction in granular layers: hysteresis and precursors. *Phys. Rev. Lett.* **79**, 949–952 (1997).
24. Alvarez, M. M., Muzzio, F. J., Cerbelli, S., Androver, A. & Giona, M. Self-similar spatiotemporal structure of intermaterial boundaries in chaotic flows. *Phys. Rev. Lett.* **81**, 3395–3398 (1998).
25. Rudolph, M., Shinbrot, T. & Lueptow, R. M. A model of mixing and transport in wavy Taylor-Couette flow. *Physica D* **121**, 163–174 (1998).
26. Shinbrot, M. Fixed-point theorems. *Sci. Am.* **214**, 105–110 (1966).
27. Scott, D. R. Seismicity and stress rotation in a granular model of the brittle crust. *Nature* **381**, 592–595 (1996).
28. Pöschel, T. & Buchholtz, V. Complex flow of granular material in a rotating cylinder. *Chaos Solitons Fractals* **5**, 1901–1912 (1995).
29. Wolf, A., Swift, J. B., Swinney, H. L. & Vastano, J. A. Determining Lyapunov exponents from a time series. *Physica D* **16**, 285–317 (1985).

**Acknowledgements.** This work was supported by the International Fine Powder Research Institute, the NSF, the New Jersey Commission on Science and Technology, and Pfizer Pharmaceuticals. We thank A. Abad for technical assistance.

Correspondence and requests for materials should be addressed to F.J.M. (e-mail: muzzio@sol.rutgers.edu).

## Self-organized growth of alloy superlattices

P. Venezuela\*, J. Tersoff†, J. A. Floro‡, E. Chason‡§, D. M. Follstaedt‡, Feng Liu\* & M. G. Lagally\*

\* Department of Materials Science and Engineering, University of Wisconsin, Madison, Wisconsin 53706, USA

† IBM Research Division, T. J. Watson Research Center, PO Box 218, Yorktown Heights, New York 10598, USA

‡ Sandia National Laboratories, Albuquerque, New Mexico 87185-1415, USA

**Patterning in nature typically occurs through self-organization, and interest has developed recently in the use of such spontaneous processes to fabricate periodically structured materials at the nanometre scale. For example, ordered arrays of semiconductor ‘quantum dot’ particles (superlattices) have been created by deposition from a suspension<sup>1</sup>, or by self-organization of diffusing atoms on surfaces<sup>2</sup> or in sequentially grown stacked layers<sup>3</sup>. The spontaneous formation of layered structures in epitaxial growth has also been reported, and attributed to the process of spinodal decomposition<sup>4,5</sup>. Yet highly ordered layered superlattices, developed for applications in optoelectronics (and in future perhaps for thermoelectrics<sup>6</sup>), are created ‘by hand’ through the sequential deposition of two different materials. Here we show that superlattices can appear spontaneously during crystal growth of an alloy, as a consequence of the**

§ Present address: Brown University, Division of Engineering, Providence, Rhode Island 02912, USA.

**distribution of strain at surface step sites. When a strained alloy grows by 'step flow', the surface steps form periodic bunches<sup>7</sup>. We find that the resulting modulated strain field biases the incorporation of the respective alloy components at different steps in the bunch, leading to segregation and superlattice formation. We also present experimental observations (X-ray diffraction and electron microscopy) of a silicon-germanium alloy grown on silicon, which show clear evidence for the formation of such a self-organized structure.**

Semiconductor devices are typically grown on a 'vicinal' surface, a staircase of atomically flat terraces separated by atomic-height steps. Atoms are deposited on the surface (by evaporation or vapour decomposition), and they diffuse as 'adatoms' on the terraces. Step motion arises from attachment or detachment of these adatoms at the step.

The adatom density on a terrace obeys the diffusion equation, subject to boundary conditions of equilibrium at the steps. Solving this equation gives the current of adatoms; the discontinuity in this current at a step gives the net attachment or detachment rate, and hence the step velocity. The physics of strain and alloying enters solely through the composition-dependent chemical potential at the steps, which determines the local adatom density and hence the adatom diffusion, step motion, and crystal growth<sup>8-10</sup>.

Recently Liu *et al.*<sup>7</sup> showed that such growth leads to periodic patterns of step bunches on the crystal surface. Here we consider growth of an alloy, in which the elements differ in their size and surface mobility. The step bunches affect the surface elastic field, giving different strains at different steps. The smaller adatoms will be incorporated preferentially at steps having relatively compressive strain, and larger adatoms at relatively tensile steps<sup>9,11</sup>. In addition, steps having lowest absolute strain are favoured overall, and atoms of the more mobile species can more readily reach these preferred steps<sup>10</sup>.

The equations describing alloy decomposition are nonlinear, and so inherently difficult to solve. We therefore consider the limit of only a small difference in size and/or mobility between the alloy elements, so that we can linearize the problem. In this case, and making use of prior results<sup>9,10</sup>, we can write the evolution of surface morphology as

$$\dot{u}_m = \frac{1}{2}(u_{m+1} - u_{m-1}) + \bar{\lambda}^3 \Phi_m \quad (1)$$

Here  $u_m = (x_m/L_{av}) - m - Ft$  is the step displacement, written for convenience in dimensionless units, relative to an ideal train of equispaced steps;  $x_m$  is the actual step position;  $L_{av}$  is the average step separation (fixed by the surface 'vicinal angle'), and  $F$  the total incident flux (the growth rate) in monolayers per unit time. (We do not include any step-edge diffusion barriers.) The corresponding dimensionless step velocity is  $\dot{u}_m = du_m/d\tau$ , where  $\tau = Ft$  is the dimensionless time. For an alloy of two components, indexed by the subscript  $\nu$ ,  $\lambda_\nu = [\exp((\bar{\mu}_\nu - E_\nu)/kT)D_\nu M\bar{\epsilon}^2\beta h/4FkT]^{1/3}/L_{av}$  characterizes the strain-driven diffusion for component  $\nu$ . Here  $\bar{\mu}_\nu$  is the average chemical potential,  $E_\nu$  and  $D_\nu$  are the energy and mobility of an adatom of component  $\nu$ ,  $T$  is the temperature,  $M$  is the product of the atomic volume and an elastic constant,  $\bar{\epsilon}$  is the misfit strain,  $\beta$  is a ratio between elastic constants, and  $h$  is the step height. Only the average  $\bar{\lambda} = (\lambda_\nu + \lambda_{-\nu})/2$  enters Equation (1), where the subscript  $-\nu$  denotes the component other than  $\nu$ . Finally,

$$\Phi_m = \frac{S_{m+1} - S_m}{u_{m+1} - u_m + 1} - \frac{S_m - S_{m-1}}{u_m - u_{m-1} + 1}$$

where  $S_m = \sum_{n \neq m} (u_m + m - u_n - n)^{-1} - l_0^2 \sum_{n \neq m} (u_m + m - u_n - n)^{-3}$ , and  $l_0$  is the minimum-energy distance between two isolated steps, in units of  $L_{av}$ .

The dynamical evolution of the surface morphology is determined by numerical integration of the step velocity, equation (1). The behaviour is controlled by two parameters,  $l_0$  and  $\bar{\lambda}$ . These

reflect respectively the short-range step repulsion and the long-range strain field (because the step changes the elastic boundary condition for the misfit strain).

The morphological evolution has been treated previously<sup>7</sup>. The new result which makes our simulation possible is the alloy decomposition at the steps:

$$\Delta c_\nu = \bar{c}_\nu \bar{c}_{-\nu} \alpha_\nu \Psi [I - \gamma \bar{\lambda}^3 A]^{-1} \quad (2)$$

Here  $\Delta c_\nu$  gives the deviation from the average composition  $\bar{c}_\nu$ . Its  $m$ th component refers to step  $m$ . The  $m$ th component of  $\Psi$  is  $\bar{\lambda}^3 \Phi_m / (1 + \dot{u}_m)$  for equal-sized atoms;  $I$  is the identity matrix; and  $A$  is a cyclic tridiagonal matrix with  $A_{m,m\pm 1} = \pm (1 + \dot{u}_m)^{-1} (u_{m\pm 1} - u_m \pm 1)^{-1}$  and  $A_{m,m} = -(A_{m,m+1} + A_{m,m-1})$ . A detailed derivation of these results will be given elsewhere.

Given the surface morphology, there are two important (and competing) terms which determine the alloy decomposition. The difference in size and mobility of the two species are reflected in the parameter

$$\alpha_\nu = 4 \frac{\Delta \epsilon_\nu}{\bar{\epsilon}} + 3 \frac{\Delta \lambda_\nu}{\bar{\lambda}} \quad (3)$$

where  $\Delta \epsilon_\nu / \bar{\epsilon}$  is the fractional misfit difference, with  $\Delta \epsilon_\nu = (a_{-\nu} - a_\nu) / a_0$ ,  $a_\nu$  and  $a_0$  being the lattice parameters of component  $\nu$  and of the substrate, respectively; and  $\Delta \lambda_\nu / \bar{\lambda}$  is the fractional difference in mobility, relative to the average, where  $\Delta \lambda_\nu = \lambda_\nu - \lambda_{-\nu}$ . We note that the effects of atomic size and mobility difference can add or partially cancel, depending on the relative signs<sup>10</sup>.

The other important parameter is

$$\gamma = \bar{c}_\nu \bar{c}_{-\nu} 4 \frac{L_{av} g''_\nu}{\beta h M \bar{\epsilon}^2} \quad (4)$$

This acts in the opposite way from  $\alpha_\nu$ , to suppress decomposition. Here  $g''_\nu$  is the second derivative, with respect to composition, of the free energy of mixing of the alloy. As long as the alloy is stable against spinodal decomposition,  $g''_\nu > 0$  and so  $\gamma > 0$ . The larger  $\gamma$  is, the

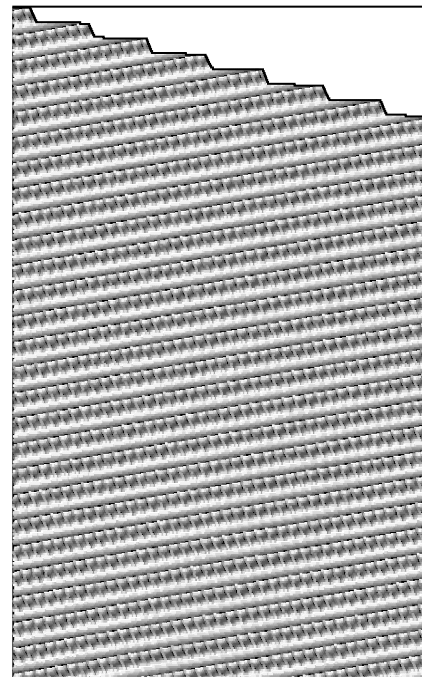


**Figure 1** Cross-sectional view of simulated superlattice formation. The parameters used in this calculation are:  $\bar{\lambda} = 0.446$ ,  $\Delta \epsilon = 0$  and  $l_0 = 0.192$ . The vertical axis has been exaggerated for clarity. The black and white regions are enriched in one or the other component, while the grey regions have composition close to the average composition.

smaller the decomposition  $\Delta c_\gamma$ . Other factors being equal, the alloy decomposition will be largest in systems where the critical temperature  $T_c$  for spinodal decomposition is not far below the growth temperature  $T$ , because  $\gamma \rightarrow 0$  as  $T \rightarrow T_c$ .

An example of the calculated growth is shown in Fig. 1, for  $l_0 = 0.192$ ,  $\Delta\epsilon = 0$ , and  $\bar{\lambda} = 0.446$ . The simulation included 120 steps, with periodic boundary conditions to eliminate end effects. The vertical axis in Fig. 1 has been exaggerated for clarity. The black and white regions are enriched in one or the other component, while the grey regions have composition close to the average value.

The result is an ordered pattern of composition modulation. We believe that this is the first actual calculation showing spontaneous superlattice formation in any system. Note the remarkable regularity of the structure, which appears to be independent of initial conditions and robust against noise. Increasing the growth rate reduces  $\bar{\lambda}$ , giving smaller bunches<sup>7</sup> and hence a shorter superlattice period. It was speculated previously, on heuristic grounds, that such decomposition would occur at step bunches<sup>9</sup>. However, owing to the collective nature of the phenomenon, and the importance of mobility differences<sup>10</sup>, the actual results here differ dramatically from earlier speculations.

Because of the combination of short-range and long-range strains around each step, the total strain (and hence the chemical potential) is higher at the top and bottom of a step-bunch, and lower in the middle. The more mobile atoms are more successful at reaching the favoured mid-bunch sites, and so are preferentially incorporated

there. The atomic size similarly biases the incorporation of the two types of atoms<sup>10</sup>.

We note that in Fig. 1 the superlattice is misorientated in relation to the crystallographic plane (horizontal direction) by an angle which is comparable to the surface vicinal angle, but in the opposite direction. This is due to the complex step dynamics, in which free steps are continually ejected from the base of a bunch and then captured by the adjacent bunch<sup>7</sup>.

We have repeated the simulation for several values of  $\gamma$ . In general, the pattern of the decomposition reflects the surface morphology, and so is unaffected by  $\gamma$ . However,  $\gamma$  has a strong effect on the magnitude of the decomposition. Near the critical temperature  $T_c$  for spinodal decomposition,  $\gamma$  is small and the decomposition is quite large. But it is difficult to evaluate  $\gamma$  for specific real systems, because  $T_c$  is not accurately known.

In Fig. 2 we show measurements of a  $\text{Si}_{0.84}\text{Ge}_{0.16}$  alloy grown by molecular beam epitaxy on Si(001) at 380 °C. The sample was grown without wafer rotation (periodic structures are sometimes created accidentally during growth by wafer rotation). The surface 'miscut', the deviation from (001) orientation, is too small to measure accurately, so the local miscut is dominated by the small deviations from planarity.

A cross-sectional transmission electron microscope (TEM) image is shown in Fig. 2a. The superlattice modulation, with a period of  $\sim 3$  nm, is clearly visible despite the 'noisiness' of the image. (Viewing the image obliquely from the side enhances the clarity.)

X-ray diffraction provides a more quantitative measure of composition modulation (Fig. 2b). Comparison with calculated diffraction intensities suggests that the absolute composition modulation is of the order of 10%. Each peak in the diffracted intensity indicates the presence of some composition modulation with the period indicated. The multiple peaks indicate the presence of several distinct periods. All are around 3 nm, consistent with the TEM. A Fourier analysis of the TEM image (not shown here) also shows multiple periods separated by  $\sim 0.3$  nm. We infer that the sample has microdomains, so that roughly speaking, each peak originates in a region having that periodicity.

We note that the separation between the principal diffraction peaks in Fig. 2b corresponds to an integer number of atomic double-layers ( $\sim 0.27$  nm). This confirms that the structure is truly self-organized, because an external perturbation would not give multiple periodicities differing by integer thicknesses.

It is not possible to prove definitely that the experiment reflects the same mechanism proposed in the theory. But because no other mechanism is known which could lead to such behaviour, the presumption is reasonable. Both our theory and our experiments are for systems that are stable against spinodal decomposition, and so are unrelated to previous observations<sup>4,5</sup> or previous heuristic theoretical discussions<sup>12,13</sup> for unstable systems. Moreover, the presence of multiple periodicities is consistent with the proposed mechanism. The average bunch size may vary across the sample owing to small differences in local surface miscut, flux or temperature. But bunches can differ only by integer numbers of steps; and if bunches of different size coexist they tend to "phase separate" into separate regions of uniform bunch size<sup>7</sup>. Such regions will have periods differing by integer numbers of atomic layers. (SiGe is well known to show step 'pairing', and the dominant spacing in Fig. 2 corresponds to the bilayer step height.)

There is still much to be understood in this system. We have not yet identified the precise experimental conditions for reproducibly growing superlattices. Also the quantitative predictions of the theory will be affected if we include other effects such as diffusion barriers, step permeability, and other step-repulsion mechanisms. But none of those would eliminate the basic morphological self-organization, and the resulting periodic modulation of the alloy composition. These appear to be very robust effects, as long as growth takes place in the step-flow mode described.  $\square$

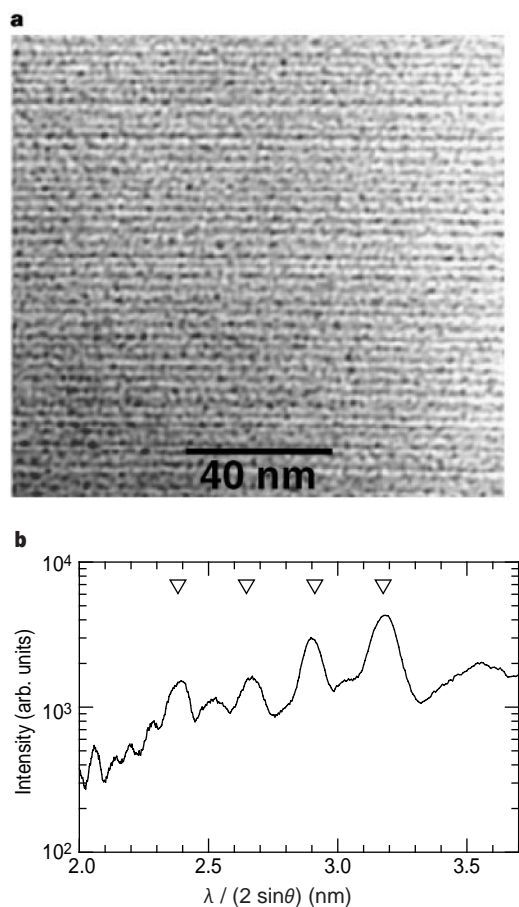


**Figure 2** Observations of superlattice formation for a  $\text{Si}_{0.84}\text{Ge}_{0.16}$  alloy grown on Si(001). **a**, Bright-field TEM image, [110] cross-section, obtained with (002) two-beam diffraction conditions. The top edge is towards the growth surface. Despite 'noise', horizontal layers with spacings around 3 nm are clearly visible. **b**, X-ray diffraction intensity (from  $\theta$ - $2\theta$  scan), versus periodicity (from X-ray wavelength  $\lambda$  and scattering angle  $\theta$ ). The arrow heads indicate successive major peaks differing by the bilayer step height.

Received 4 September; accepted 9 December 1998.

- Murray, C. B., Kagan, C. R. & Bawendi, M. G. Self-organization of CdSe nanocrystallites into three-dimensional quantum dot superlattices. *Science* **270**, 1335–1338 (1995).
- Shchukin, V. A., Ledentsov, N. N., Kop'ev, P. S. & Bimberg, D. Spontaneous ordering of arrays of coherent strained islands. *Phys. Rev. Lett.* **75**, 2968 (1995).
- Tersoff, J., Teichert, C. & Lagally, M. G. Self-organization in growth of quantum dot superlattices. *Phys. Rev. Lett.* **76**, 1675–1678 (1996).
- Petroff, P. M., Cho, A. Y., Reinhart, F. K., Gossard, A. C. & Wiegmann, W. Alloy clustering in Ga<sub>1-x</sub>Al<sub>x</sub>As compound semiconductors grown by molecular beam epitaxy. *Phys. Rev. Lett.* **48**, 170–173 (1982).
- Norman, A. G., Seong, T. Y., Ferguson, I. T., Booker, G. R. & Joyce, B. A. Structural studies of natural superlattices in group III–V alloy epitaxial layers. *Semicond. Sci. Technol.* **8**, S9–S15 (1993).
- Mahan, G. D. & Woods, L. M. Multilayer thermionic refrigeration. *Phys. Rev. Lett.* **80**, 4016–4019 (1998).
- Liu, F., Tersoff, J. & Lagally, M. G. Self-organization of steps in growth of strained films on vicinal substrates. *Phys. Rev. Lett.* **80**, 1268–1271 (1998).
- Tersoff, J., Phang, Y. H., Zhang, Z. & Lagally, M. G. Self-bunching instability of vicinal substrates under stress. *Phys. Rev. Lett.* **75**, 2730–2733 (1995).
- Tersoff, J. Stress-driven alloy decomposition during step-flow growth. *Phys. Rev. Lett.* **77**, 2017–2020 (1996).
- Venezuela, P. & Tersoff, J. Alloy decomposition during growth due to mobility differences. *Phys. Rev. B* **58**, 10871–10874 (1998).
- Guyer, J. E. & Voorhees, P. W. Morphological stability of alloy thin films. *Phys. Rev. Lett.* **74**, 4031–4034 (1995).
- Barabási, A. Self-organized superlattices formation in II–IV and III–V semiconductors. *Appl. Phys. Lett.* **70**, 764–766 (1997).
- Tersoff, J. Spinodal decomposition during step-flow growth. *Phys. Rev. B* **56**, R4394–R4397 (1997).

**Acknowledgements.** P.V. was supported by the Brazilian agency FAPESP.

Correspondence and requests for materials should be addressed to J.T. (e-mail: tersoff@us.ibm.com).

## Non-aqueous supramolecular assembly of mesostructured metal germanium sulphides from (Ge<sub>4</sub>S<sub>10</sub>)<sup>4-</sup> clusters

Mark J. MacLachlan, Neil Coombs & Geoffrey A. Ozin

Materials Chemistry Research Group, Department of Chemistry, 80 St George Street, Toronto, Canada M5S 3H6

Microporous materials have found extensive application as catalysts, ion-exchange media and sorbents<sup>1,2</sup>. The discovery of mesoporous silica<sup>3</sup> has opened the path to selective catalysis and separation of large molecules and to the synthesis of inorganic–organic composite materials, polymer mesofibres and semiconducting quantum dots<sup>4–7</sup>. Various oxide-based mesoporous materials, such as TiO<sub>2</sub>, ZrO<sub>2</sub>, SnO<sub>2</sub>, Al<sub>2</sub>O<sub>3</sub>, Nb<sub>2</sub>O<sub>5</sub> and GeO<sub>2</sub>, have been reported<sup>8–13</sup>. A challenge for materials research is now to expand the scope of mesoporous materials beyond the oxides. Only a few non-oxide mesostructured composites, such as CdS, SnS<sub>2</sub> and CdSe, have been reported; they are usually synthesized by *ad hoc* hydrothermal methods or from aqueous solutions containing ill-defined species, and are often not well characterized<sup>14–16</sup>. Here we report the rational synthesis of a new family of metal germanium sulphide mesostructured materials prepared by a non-aqueous surfactant-templated assembly of adamantanoid [Ge<sub>4</sub>S<sub>10</sub>]<sup>4-</sup> cluster precursors. In the presence of quaternary alkylammonium surfactants, [Ge<sub>4</sub>S<sub>10</sub>]<sup>4-</sup> anions in formamide solution self-organize with metal cations (Co<sup>2+</sup>, Ni<sup>2+</sup>, Cu<sup>+</sup> and Zn<sup>2+</sup>) to create well ordered hexagonal metal germanium sulphide mesostructures, some having fibre-like morphologies with channels running down the long axis of the fibre. Materials of this genre could prove effective in applications as diverse as detoxification of heavy metals in polluted water streams, sensing of sulphurous vapours, and the formation of semiconductor quantum ‘anti-dot’ devices.

Open-framework metal germanium sulphides with ordered micropores are a class of materials in which the metal, chalcogenide and template molecules may be varied to ‘tune’ the pore size and properties of the resulting structure<sup>17–23</sup>. In water, metal ions

assemble with anionic [Ge<sub>4</sub>S<sub>10</sub>]<sup>4-</sup> adamantanoid clusters in the presence of tetramethylammonium (TMA) cations to give crystalline metal germanium sulphide microstructured materials<sup>19</sup>. We identified this approach as a modular assembly route to metal germanium sulphide mesostructured materials. But to achieve this goal the surfactant, [Ge<sub>4</sub>S<sub>10</sub>]<sup>4-</sup> and metal precursors must be soluble and assemble into mesophases in water. Unfortunately, precursors like CTA<sub>4</sub>Ge<sub>4</sub>S<sub>10</sub> (where CTA is cetyltrimethylammonium) are sparingly soluble in water. With these restrictions in mind, we chose formamide as a solvent for the preparations because it will dissolve all of the reagents, and because the binary phase diagram of surfactants in formamide resembles that of water<sup>24</sup>.

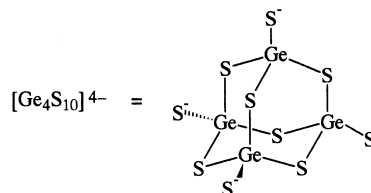


Figure 1a shows a typical powder X-ray diffractogram of the mesostructured Ni/[Ge<sub>4</sub>S<sub>10</sub>]<sup>4-</sup> material prepared according to the procedures outlined in the Methods section. The product displays four reflections consistent with diffraction from a hexagonal unit cell with dimension  $a = 39.5 \text{ \AA}$ , attesting to the high degree of order of this material. Moreover, the diffraction pattern reveals no evidence for crystalline materials that would be expected from residual surfactant or dense phases. Powder X-ray diffractograms of the analogous Zn, Cu and Co materials are shown in Fig. 1b. Although they do not appear to be as well ordered as the Ni/[Ge<sub>4</sub>S<sub>10</sub>]<sup>4-</sup> products, we attribute the broadening of the peaks and the overlap of the 110 and 200 reflections in these materials to small particle sizes (less than  $\sim 200 \text{ nm}$ ). Indeed, transmission electron microscopy (TEM) suggests that many of these samples are better ordered than their nickel analogue, though the particles are clearly smaller.

TEM images of whole-mounted samples are shown in Fig. 1c–f. Hexagonal mesoscopic ordering of the materials extends over entire particles constituting the samples; overall, the samples appear homogeneous when viewed under the electron microscope. Energy-dispersive X-ray analysis of single mesostructured particles confirmed the presence of germanium, sulphur and the metal. Worm-like morphologies (Fig. 1e–f) have been observed by TEM.

Raman spectroscopy of the mesostructured materials confirms the presence of metal-linked adamantanoid clusters. Figure 2A, trace a, shows the Raman scattering from a sample of (CTA)<sub>4</sub>Ge<sub>4</sub>S<sub>10</sub> containing the molecular cluster<sup>25</sup>. In particular, the spectrum displays two sets of modes due to Ge–S stretching: (1) terminal Ge–S<sub>t</sub> modes between 340 and 480 cm<sup>-1</sup>; and bridging Ge–S<sub>b</sub> modes between 160 and 230 cm<sup>-1</sup>. The symmetric Ge–S<sub>t</sub> stretching mode observed at 342.0(±0.1) cm<sup>-1</sup> has a full-width at half-maximum (FWHM) of 7.6(±0.6) cm<sup>-1</sup>. For comparison, the Raman spectrum of the crystalline TMA<sub>2</sub>ZnGe<sub>4</sub>S<sub>10</sub> microstructure, in which the [Ge<sub>4</sub>S<sub>10</sub>]<sup>4-</sup> clusters are intact and linked by tetrahedral metal sites, is shown in Fig. 2A, trace b. In the crystalline framework structure, the symmetric mode shifts to 350.7(±0.2) cm<sup>-1</sup> but the linewidth of this peak remains virtually unchanged (FWHM, 8.8(±0.5) cm<sup>-1</sup>). We note that weak modes attributed to Zn–S stretching are present between 250 and 320 cm<sup>-1</sup>. Figure 2A, trace c, shows the Raman spectrum of a sample of the mesostructured Zn/[Ge<sub>4</sub>S<sub>10</sub>]<sup>4-</sup> material. The symmetric Ge–S<sub>t</sub> stretching mode is observed at 350.7(±0.2) cm<sup>-1</sup> with a FWHM of 19(±2) cm<sup>-1</sup>. Moreover, the other Ge–S<sub>t</sub> and Ge–S<sub>b</sub> modes in the mesostructured material resemble those of the linked microstructure (Fig. 2A, trace b) but are much broader. A congested region of overlapping vibrational modes between 240 and 320 cm<sup>-1</sup> are Zn–S stretching modes, as observed in linked microstructured Zn/[Ge<sub>4</sub>S<sub>10</sub>]<sup>4-</sup> materials. These results are consistent with metal-linked [Ge<sub>4</sub>S<sub>10</sub>]<sup>4-</sup> clusters present in a number of sites, where the